

Thermal characteristics and corrosion behaviour of Mg–xZn alloys for biomedical applications

AMIR FEREIDOUNI LOTFABADI^{a,b,*}, MOHD HASBULLAH IDRIS^b, ALI OURDJINI^b,
MOHAMMED RAFIQ ABDUL KADIR^c, SAEED FARAHANY^b and HAMID REZA
BAKHSHESHI-RAD^b

^aDepartment of Manufacturing and Industrial Engineering, Faculty of Mechanical Engineering,
Universiti Teknologi Malaysia, 81310 Johor Bahru, Johor, Malaysia

^bDepartment of Materials Engineering, Faculty of Mechanical Engineering, Universiti Teknologi Malaysia,
81310 Johor Bahru, Johor, Malaysia

^cDepartment of Biomechanics and Biomedical Materials, Faculty of Biomedical Engineering and Health Sciences,
Universiti Teknologi Malaysia, 81310 Johor Bahru, Johor, Malaysia

MS received 30 April 2012; revised 1 August 2012

Abstract. The thermal parameters of Mg–xZn cast alloys with 0.5–9 wt% Zn were evaluated by using computer aided cooling curve thermal analysis (CA–CCTA), whereas the corrosion behaviour was investigated by potentiodynamic polarization and immersion tests. Thermal analysis results revealed that the dendrite coherency temperature (T_{DCP}) decreased from 642.2 to 600 °C with the addition of Zn from 0.5 to 9 wt%. The liquid fraction at coherency point (f_L^{DCP}) increased by 72% when Zn was increased up to 9 wt%. MgZn intermetallic phase was observed in samples with <3 wt% Zn. At higher percentages of Zn, the Mg₅₁Zn₂₀ intermetallic phase was also detected in addition to α -Mg and MgZn by first derivative cooling curves under non-equilibrium solidification. All these phases were observed along the grain boundary when Zn was rejected from the solid/liquid interface and enriched in the triple conjunction of grain boundary. The grain size decreased from 185.2 to 71.5 μ m when Zn content was increased. The addition of Zn content had a significant effect on the corrosion rate and the corresponding mechanisms. The corrosion rate decreased from 2.1 to 1.81 mmpy as Zn content increased from 0.5 to 3 wt%; afterwards, however, this value increased with further increase of Zn. Mg–3Zn also had the lowest degradation rate and highest corrosion resistance which can be fully utilized for biodegradable orthopedic applications.

Keywords. Thermal analysis; corrosion behaviour; microstructure.

1. Introduction

Research and development of biodegradable materials has attracted a great deal of attention in recent years because of their importance in supporting tissue revival and healing which takes place by degradation of the biodegradable implant material and its replacement by the tissue (Witte *et al* 2008). In contrast to the current biodegradable materials based on ceramics, polymers or bioactive glasses, biodegradable metallic biomaterials exhibit superior behaviour in load-bearing applications due to their higher tensile strength and Young's modulus (Wen *et al* 2004; Witte *et al* 2006, 2007). In recent years, investigation on corrosion behaviour and mechanical properties of magnesium alloys has assumed great importance (Ren *et al* 2005; Witte *et al* 2005; Song 2007; Somekawa *et al* 2009). Understanding the interfacial interaction between magnesium alloys and biological environment of the implanted area has been one of the major advances in research of biodegradable magnesium biomaterials. In contrast to earlier alloy development aimed at

improving the mechanical properties, corrosion resistance and reducing cost of production of Mg alloys, the effect of alloying elements on the evolution of corrosion protective interface has been the main focus recently.

Recently, research work has reported an investigation on the possibility of using magnesium alloys in biomedical applications such as cardiovascular magnesium stents in animals (Waksman *et al* 2005, 2006). Di-Mario *et al* (2004), Erbel *et al* (2007) and Waksman *et al* (2009) reported that the first clinical human trials have been conducted. Use of Mg alloys as bone implants in various designs such as screws, plates and other types of fixture devices have also been investigated (Xu *et al* 2007; Zhang *et al* 2010). In addition, Mg alloys were also investigated as load bearing biomaterials for tissue engineering (Witte *et al* 2005, 2006, 2007), while Mg alloys shaped in the form of chips were also investigated for vertebral fusion in spinal surgery (Kaya *et al* 2007). It has also been reported that a high extracellular magnesium concentration may be helpful for cartilage tissue engineering (Feyerabend *et al* 2006).

Magnesium alloys exhibit lower elastic modulus and higher yield strength compared to metallic implants that are

*Author for correspondence (fereidouni.a@gmail.com)

currently in use (Rosalbino *et al* 2010). However, their low corrosion resistance have prevented these alloys to be used as permanent medical implants. Thus, in order to maximize their potential use in biomedical applications, it is essential to improve their corrosion resistance and control the degradation rate (Song and Song 2006; Harandi *et al* 2011).

Indeed, previous research (Heublein *et al* 2003; Lévesque *et al* 2003; Alvarez-Lopez *et al* 2010; Stulikova and Smola 2010; Zhang *et al* 2010; Yu *et al* 2012) have shown that some of these alloys possess improved corrosion behaviour and can thus be considered as biocompatible materials. Most of the reported biodegradable magnesium alloys contain aluminum and rare-earth (RE) elements that are harmful to the human body. For example, Al^{3+} ions cause phosphate leakage bodies because it combines with inorganic phosphates. Elevated concentrations of Al^{3+} in the brain are related with Alzheimer's disease (Ku *et al* 2002; El-Rahman 2003). Additionally, presence of RE elements (Pr, Ce, Y, etc.) could lead to hepatotoxicity. Unwarranted yttrium ions (Y^{3+}) caused changes in the appearance of some rat genes and are believed to negatively affect DNA transcription factors (Yumiko *et al* 1997; Yang *et al* 2006). Zinc, on the other hand, is an essential nutritional element in the body and shows appropriate non-toxicity for biomedical applications (Zhang *et al* 2010). In addition to increasing the corrosion resistance of magnesium alloys, zinc also has a significant effect on the mechanical properties (Haferkamp *et al* 2003; Song 2007; Xu *et al* 2007; Somekawa *et al* 2009).

As alternative biodegradable biomaterials, various tertiary Mg–Zn–X alloys have been investigated recently but very little work has been conducted on binary Mg–Zn alloys. Zhang *et al* (2010) studied *in vitro* and *in vivo* Mg–Zn alloys and from their results they argued that an amount of 6.2 wt% Zn is considered an appropriate content based on Mg–Zn binary phase diagram (Okamoto 1994). With regard to non-equilibrium solidification, different intermetallic phases are formed in Mg–Zn alloy, which significantly affect the corrosion behaviour. The formation of these intermetallic phases depends mostly on the amount of Zn added to the alloy. Research on the relationship between the formation of these intermetallic phases and Zn content has been lacking. Also little is known on the effect of Zn content on the microstructure and corrosion behaviour of Mg–xZn binary alloys. Thus, the aim of the present paper is to report results of an investigation of *in vitro* degradation, corrosion properties and solidification behaviour of Mg–xZn alloys solidified under non-equilibrium conditions.

2. Materials and methods

Mg–Zn ($x = 0.5, 1.5, 3, 6$ and 9 by weight percentage) were prepared by melting pure magnesium ingots (99.99%) and pure zinc chips (99.99%). The materials were melted in an electrical resistance furnace under argon gas atmosphere in a mild steel crucible at $750\text{ }^{\circ}\text{C}$. The

molten metal was maintained at this temperature for about 45 min for stabilization. The molten alloys with different percentages of Zn were stirred for 30 s before being poured into mild steel moulds which had been preheated at $400\text{ }^{\circ}\text{C}$.

Specimens of $15 \times 15 \times 10$ mm size were then cut from the cast alloys ingots for metallographic examination. The specimens were prepared according to standard metallographic procedures of grinding, polishing and etching. Microstructure analysis to examine phase formation and morphologies of the alloys were performed using optical microscopy and scanning electron microscopy equipped with energy-dispersive X-ray spectroscopy (EDS) analysis. X-ray diffraction (XRD) was used to identify the phases that were formed. In order to evaluate the effect of Zn additions on the hardness alloys, Vickers microhardness test was conducted with applying a 5 kg force.

Characteristics of temperature and time for each phase reaction as well as the solidification behaviour of Mg–xZn alloy were determined using thermal analysis. Thermal analysis was carried out by inserting two thermocouples based on the work of Backerud *et al* (1990). The first K-type thermocouple was inserted in the centre and the second one adjusted to the wall of the preheated steel mould with dimensions of 50×40 mm (height \times diameter). The top and bottom parts of the mould were isolated by Fiberfax plates of 25 mm thickness to ensure thermal isolation during solidification. EPAD-Th8-K high-speed data acquisition system linked to DEWESoft.7 was used to obtain temperature–time data. The cooling and first derivative curves were plotted by applying FlexPro.8 data analysis software. Subsequently, the temperature between the central and wall thermocouples ($\Delta T = T_C - T_W$) was established.

To investigate the corrosion behaviour in *in vitro* conditions, samples were cut and mechanically ground using silicon carbide papers with grit size ranging from 320 to 2000. The ground samples were then washed with distilled water, rinsed and degreased ultrasonically with ethanol, then dried at room temperature for immersion test. The prepared samples were immersed into beakers containing 200 ml Kokubo simulated body fluid (SBF) (Na 142.0, K 5.0, Ca 2.5, Mg 1.5, HCO_3 4.2, Cl 147.8, HPO_4 1.0 and SO_4 0.5 mmol/L). The pH value of the solution for each sample was measured at 12 h intervals during the immersion test. The procedure of the immersion test was performed according to ASTM-G31-72 standard. The immersion test was conducted at the temperature of $37\text{ }^{\circ}\text{C}$ for 144 h. After immersion for 144 h, the samples were taken out of SBF solution and corrosion products were removed using 20% CrO_3 + 1% AgNO_3 boiling solution. Samples were then rinsed in ethanol, dried in air and finally weighed (Yin *et al* 2008). Electrochemical potentiodynamic polarization test in Kokubo solution was conducted at pH 7.66 and temperature of $37\text{ }^{\circ}\text{C}$ under air atmosphere. A three-electrode cell, consisting of graphite as the counter electrode, specimen as the working electrode and saturated calomel electrode (SCE) as the reference electrode, was used for the test. The potential scanning rate was fixed at 0.5 mV/s

for all specimens with initial potential at -250 mV below the open circuit potential.

3. Results and discussion

3.1 Microstructure observation and results

Figure 1 shows optical micrographs of as cast Mg– x Zn ($x = 0.5, 1.5, 3, 9$ in weight percentage) alloys, respectively. It

can be seen that the microstructure is composed of α -Mg and secondary phases which precipitated along the grain boundaries. In addition, it can also be observed that the grain size of Mg decreases with increasing Zn content. For instance, by increasing the Zn content from 0.5 to 3 wt%, the grain size decreased from 185.2 to 135.5 μm . With further increase of Zn content up to 9%, a reduction of 53% in grain size was obtained compared to the Mg–3Zn alloy.

The optical microstructures are confirmed by SEM micrographs shown in figure 2 (1.5% (a), 3% (b)). The

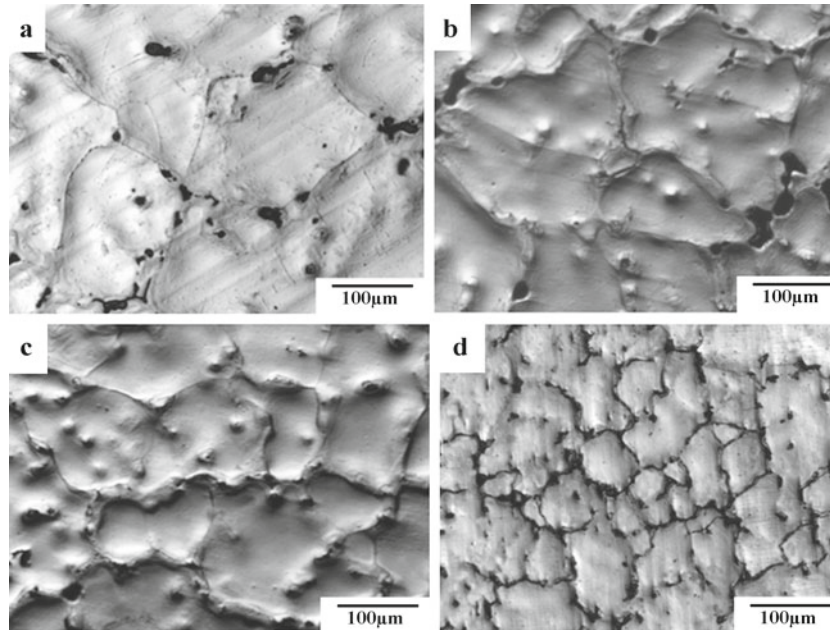


Figure 1. Optical microscopy observation for Mg– x Zn : (a) 0.5 wt% Zn, (b) 1.5 wt% Zn, (c) 3 wt% Zn and (d) 9 wt% Zn.

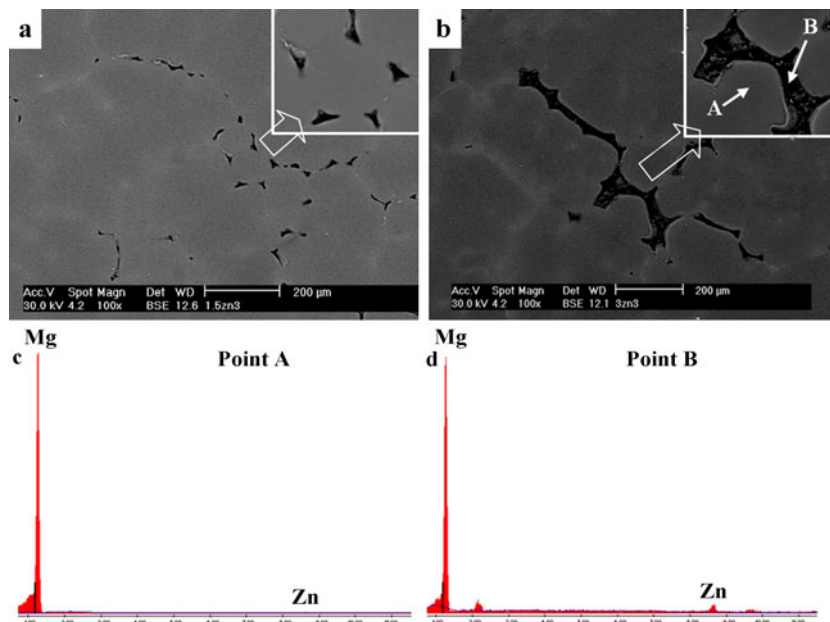


Figure 2. SEM and EDS observation of Mg–Zn alloy with (a) 1.5 wt% and (b) 3 wt% Zn content.

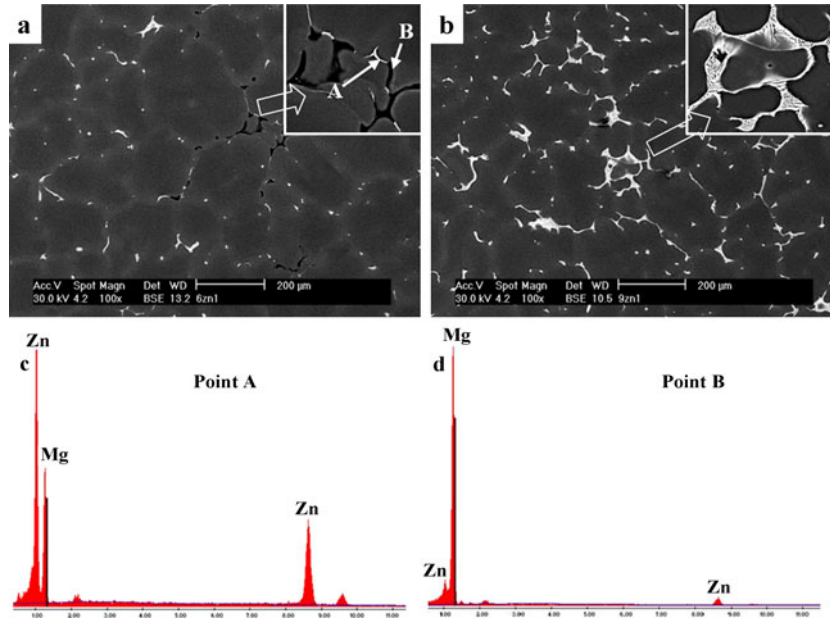


Figure 3. SEM and EDS observation of Mg–Zn alloy with (a) 6 wt% and (b) 9 wt% Zn content.

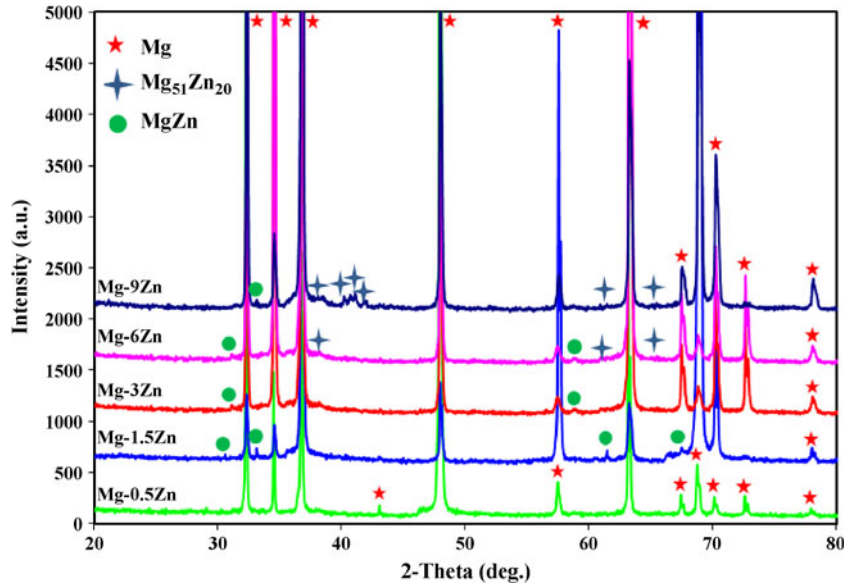


Figure 4. XRD pattern of as-cast samples of Mg–Zn alloy.

corresponding EDS analysis also confirms that the dark area that is composed of Mg and Zn is related to the evolution of MgZn phase. The fraction of this MgZn phase is increased with increasing Zn in the alloy and became non-uniformly distributed as shown in figure 2(a and b). This is evident from the fact that Zn is concentrated in the secondary phase formed along the grain boundaries which also results in Mg matrix being depleted of Zn. This is confirmed by EDS analysis of point A in figure 2(c), where the Zn concentration is

only 2.04 wt% compared with that of point B in figure 2(d) where Zn is 10.26 wt%.

Figure 3(a and b) shows a distinct phase distributed at the grain boundaries (bright phase) in addition to previous phases (dark phase MgZn) in 6 and 9 wt%, respectively. EDS analysis of the bright phase in Mg–6Zn alloy at point A in figure 3(c) indicates the presence of Zn with a value of 46.40 wt%, which suggests the formation of Mg₅₁Zn₂₀ intermetallic phase. This phase emerged in the form of eutectic

phase with lamellar structure for more than 6 wt% Zn at grain boundaries (figure 3b). Thickness of the lamellar structure appears to have increased significantly with increasing Zn

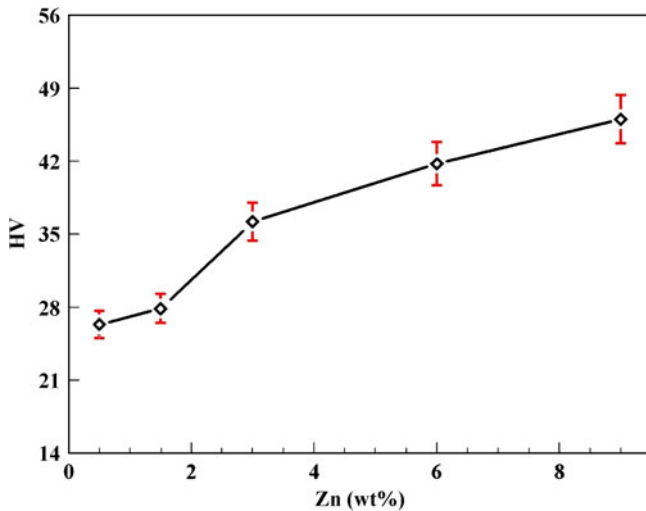


Figure 5. Effect of different Zn additions on microhardness properties of Mg–*x*Zn alloy.

content at the grain boundaries. EDS analysis of Mg–6Zn alloy at point B in figure 3(d) also indicates the presence of Zn with a value of 10.34%, confirmed the formation of MgZn phase similar to that observed in alloys of Mg–1.5Zn and Mg–3Zn.

The microstructural observations discussed above were confirmed by XRD results as shown in figure 4, for the as-cast samples of Mg–Zn alloy. In addition to the defined Mg reflections, two more peaks were observed. It can be seen that the reflection of MgZn intermetallic phase appeared in Mg–1.5Zn and Mg–3Zn. However, by further addition of Zn content, a new phase was detected in addition to the previous MgZn phase. Mg₅₁Zn₂₀ phase was enriched with Zn which confirmed SEM and EDS observation of the same samples.

The effect of the addition of different Zn contents on the microhardness of Mg–*x*Zn alloy is shown in figure 5. It was obvious that the hardness values increase with increasing Zn content for all the samples. This can be attributed to the refinement role of Zn on Mg alloys. However, for less than 3 wt% Zn addition to Mg–Zn alloy, hardness improves due to the solid solution strengthening mechanism of Zn dissolved in Mg matrix. In cases of more than 3 wt% Zn addition, the evolution of secondary phase at the grain boundary in the form of Mg₅₁Zn₂₀ in addition to MgZn intermetallic phase can be related to hardness enhancement (Yin *et al* 2008).

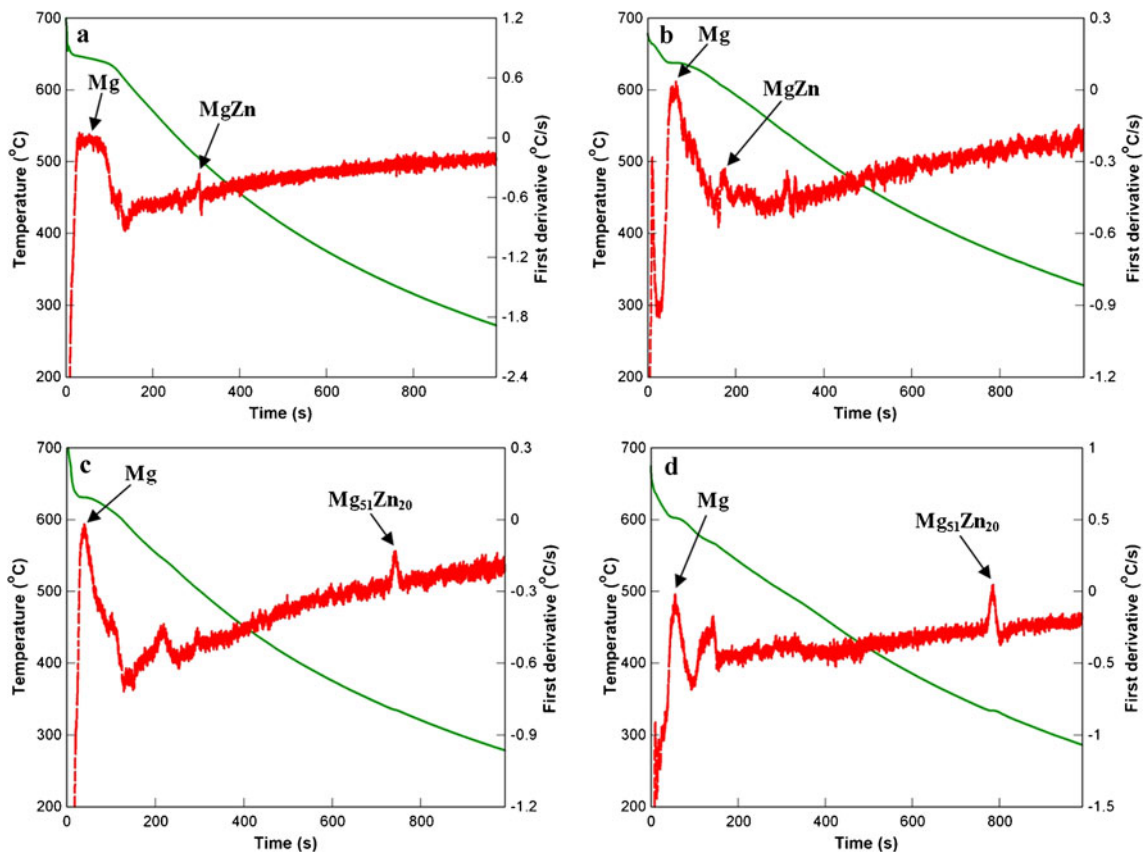


Figure 6. Cooling curves and corresponding first derivative curves of Mg–*x*Zn alloys: (a) 0.5 wt%, (b) 3 wt%, (c) 6 wt% and (d) 9 wt% Zn.

3.2 Solidification and phase transformation

Analysis of the obtained cooling curves was conducted to identify the phase evolution of α -Mg and MgZn intermetallics during solidification of Mg- x Zn systems. Both cooling curves and the corresponding first derivative curves were plotted so that the dendrite coherency point, liquid fraction percentage, characteristic temperature and time are determined. Figure 6(a) shows cooling behaviour of Mg-0.5Zn during solidification and it is clear that the formation of α -Mg and MgZn phases occurred at two different temperatures according to the following equation:

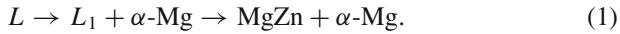


Figure 6(a) shows that α -Mg and MgZn were formed at 649.6 and 509.1 °C, respectively. Similar solidification behaviour was observed for alloys of Mg-1.5Zn and Mg-3Zn with the formation of α -Mg and MgZn at temperatures of 640.1 and 507.8 °C, respectively for Mg-3Zn alloy as shown in figure 6(b). According to the binary Mg-Zn equilibrium phase diagram (Okamoto 1994), only α -Mg is expected to form under equilibrium solidification. However, the detection of MgZn is likely due to non-equilibrium solidification and rejection of Zn solute into the solidification front. This observation suggests that MgZn is formed during the last stage of solidification in the residual melt at the interdendritic space.

Figure 6(c) indicates that during solidification of Mg-6Zn alloy, an additional new phase believed to be $\text{Mg}_{51}\text{Zn}_{20}$ was formed and compared with alloys containing <6 wt% Zn. As shown in the plot, α -Mg, MgZn and $\text{Mg}_{51}\text{Zn}_{20}$ were detected at 636.2, 597.3 and 337.5 °C, respectively. Similar results were also observed in alloy Mg-9Zn with $\text{Mg}_{51}\text{Zn}_{20}$ intermetallic phase being formed at 335.6 °C.

Figure 7 shows profile of temperature difference between the two thermocouples located at the wall and centre of the mould. This method was used in the current study to evaluate dendrite coherency point (DCP), corresponding coherent temperatures (T_{DCP}) and times (t_{DCP}) as well as liquid fraction at DCP with different Zn contents. Based on this approach, DCP occurred at the first detected maximum temperature difference between the centre and the wall thermocouples ($\Delta T = T_{\text{W}} - T_{\text{C}}$) during the formation of α -Mg. Figure 7 also demonstrates a drop in ΔT , which indicates dendrite coherency point in all Mg- x Zn specimens as a result of the enhanced thermal contact through the solid dendrite network.

It is shown that DCP occurred at 642.2 °C in 94.5 s and 640.5 °C in 94 s for Mg-0.5Zn and Mg-1.5Zn alloys, respectively. With addition of 3 wt% Zn, however, T_{DCP} decreased to 632 °C and t_{DCP} slightly increased to 97.1 s for Mg-3Zn alloy. T_{DCP} and t_{DCP} for Mg-6Zn were measured at 630 °C and 46.9 s. These characteristic parameters decreased to 600 °C and 70.2 s, respectively with the further addition

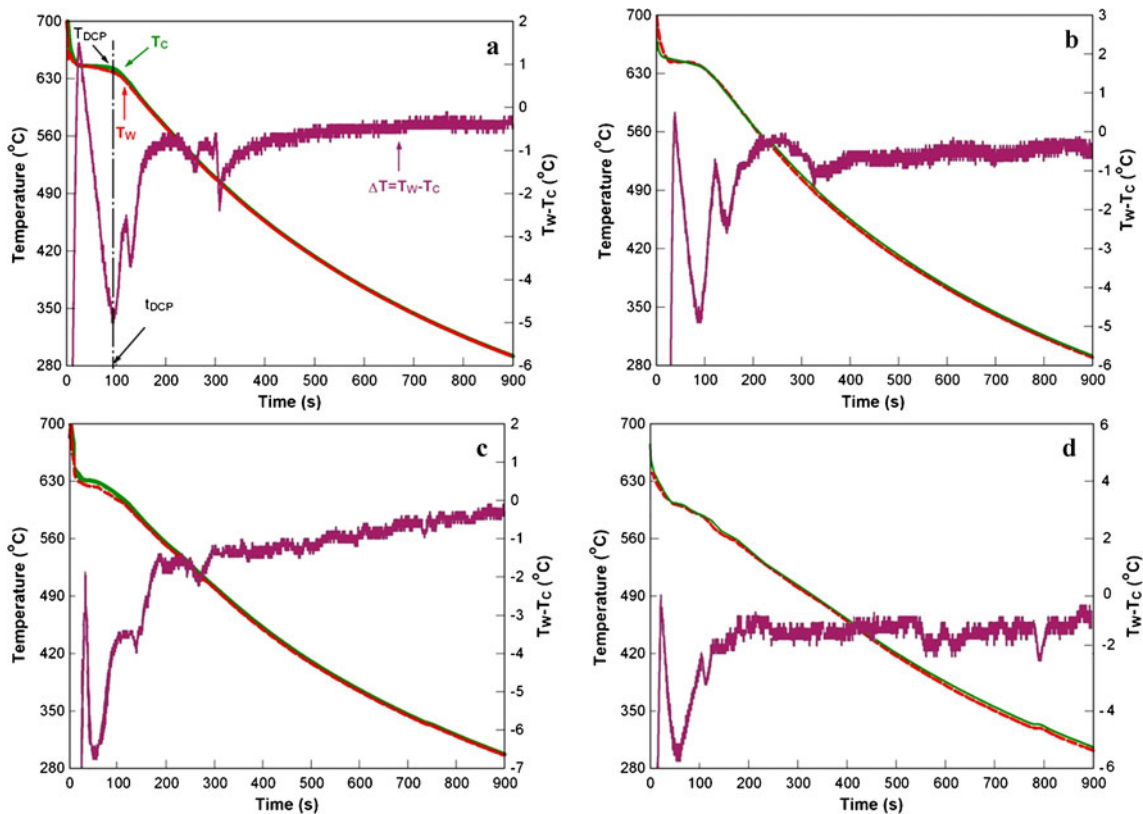


Figure 7. DCP of Mg- x Zn alloys: (a) 0.5 wt%, (b) 3 wt%, (c) 6 wt% and (d) 9 wt% Zn.

of Zn up to 9 wt%. The results clearly show that t_{DCP} did not change remarkably for 0.5–3 wt%, while it decreased for 6–9 wt% representing the role of Zn in refining of Mg grain size which confirms the results of microstructure observation.

Mg–Zn binary phase diagram shows that slope of liquidus is around $6.04\text{ }^{\circ}\text{C}/\text{wt}$ indicating the ability of Zn to hinder the growth of α -Mg dendrite size. Therefore, the grain refinement induced by addition of Zn can be explained by the growth restriction theory of solute in the Mg melt (Lee *et al* 2000). Additionally, the solidification temperature range ($\Delta T = T_s - T_f$) increases to 88% and total solidification time rises to 157%, when Zn content is increased from 0.5 up to 9 wt% Zn.

A base line was plotted for computing solid fraction at DCP for Mg– x Zn alloys. The base line has been estimated by curve fitting; the data between the onset and end of solidification in the first derivative curve, using a cubic square function as per the following equation:

$$\left(\frac{dT}{dt}\right)_z = a + bT + cT^2 + dT^3. \quad (2)$$

It should be noted that liquid fraction can be measured according to the following equation:

$$f_L = 100 - f_S. \quad (3)$$

Based on (3), f_L is found to be 43% for 0.5 wt% Zn content and this value increased to 49 and 58% for 1.5 and 3 wt% Zn additions, respectively. When Zn is increased to 9 wt%, f_L increased to 74%. This indicates that the residual liquid volume fraction increased at DCP with increasing Zn addition due to the growth restriction effect of Zn on the growth of Mg dendrites.

3.3 Immersion test

Increase in pH values causes haemolysis of about 66% (Bakhsheshi-Rad *et al* 2012), which is not suitable for proliferation and cell growth. Thus, it is important that the pH values of samples immersed in SBF solution should be monitored throughout the immersion test. The pH variations of SBF with different Zn additions vs immersion time are shown in figure 8. It is evident from the graph that pH values of the samples during the immersion test initially increased from 7.66 to 8.70, which is likely caused by the release of OH ions into the solution. However, with increased immersion time, the pH value of all specimens exhibited a constant trend due to the formation of Mg(OH)₂ and precipitation of calcium phosphate on Mg(OH)₂ and the surface of Mg–Zn alloys as shown in figure 9.

Figure 9 shows corrosion morphologies of Mg– x Zn specimens after immersion in Kokubo solution for 144 h using SEM. Figure 9(a) reveals that cracks with uniform distribution formed on Mg–0.5Zn and the formation of cracks could be attributed to dehydration of the layer after drying in an ambient atmosphere. EDS analysis in figure 10 shows that the precipitates are composed of little amounts of Ca and P

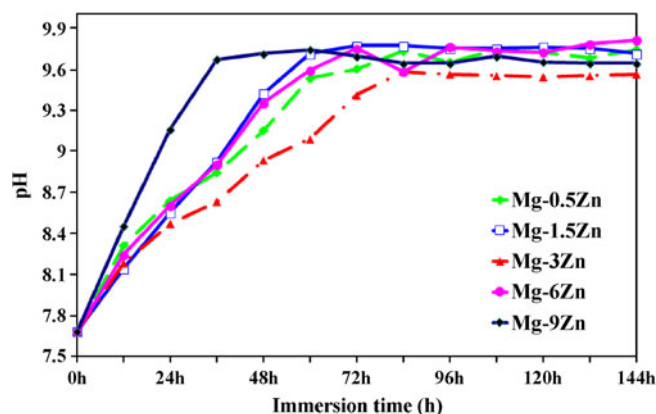
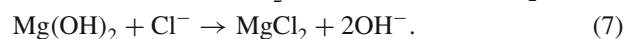
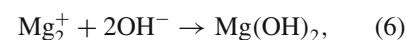
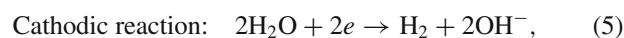
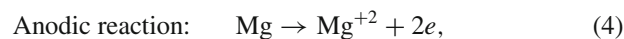


Figure 8. pH variation of SBF for Mg– x Zn alloys with different zinc contents.

and a high amount of Mg (point A), whereas the crack layer consisted mainly of high amounts of Ca and P and a little amount of Mg (point B).

It is also clear from figure 9(e) that homogeneous corrosion product precipitates on the surface of Mg–3Zn alloy. Generally, when exposed to SBF solution, Mg alloys are reactive, generating Mg²⁺ rich interface at which these extra Mg ions between the sample and solution serve to prevent nucleation of calcium phosphate deposition (Song *et al* 2010). The formation of corrosion product follows the below reactions:



Mg transforms to stable Mg²⁺ ion; subsequently the cathodic reaction occurs at the same time by formation of hydroxide ion according to reactions (4) and (5).

Mg ion reacts with hydroxide ion and forms magnesium hydroxide. By evolution of Mg(OH)₂ as a barrier layer, the degradation rate of the sample declines and corrosion products such as CO₃²⁻, PO₄³⁻ and Cl⁻ ions are precipitated on the surface of the specimen. Based on (7), chlorine reacts with the deposited Mg(OH)₂ on the specimens and forms MgCl₂ with higher solubility compared to Mg(OH)₂. Cl⁻ ions can decrease the corrosion resistance of the specimens. Moreover, Cl⁻ ion can easily penetrate the deposition layer due to its small radius which causes preferential adsorption and OH⁻ replacement by Cl⁻ (Wang *et al* 2010). As the reaction progresses, high amounts of Mg²⁺ are dissolved and as a result more HCO₃ and HPO₄ are consumed causing a decrease in the corrosion rate.

From figure 9(g and j), it can be seen that the thickness of the calcium phosphate film gradually increases with increasing the amount of Zn to 6 and 9 wt%. For Mg–6Zn alloy, corrosion attack takes place in the eutectic (Mg+Mg₅₁Zn₂₀) which relates to galvanic corrosion between the cathodic

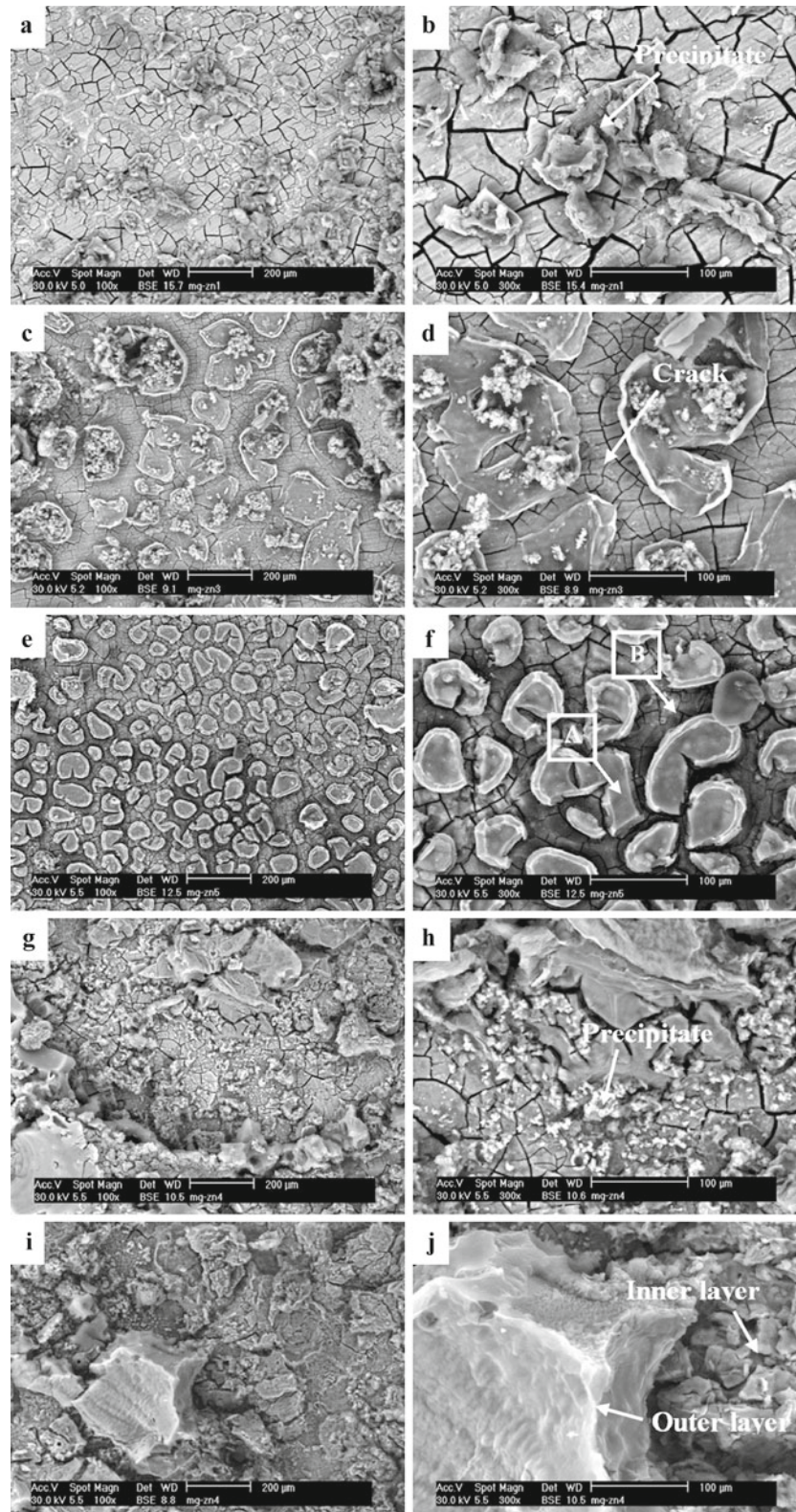


Figure 9. SEM micrographs of Mg–Zn alloys with different zinc contents: (a, b) 0.5, (c, d) 1.5, (e, f) 3, (g, h) 6 and (i, j) 9 wt% with immersion duration of 144 h in SBF.

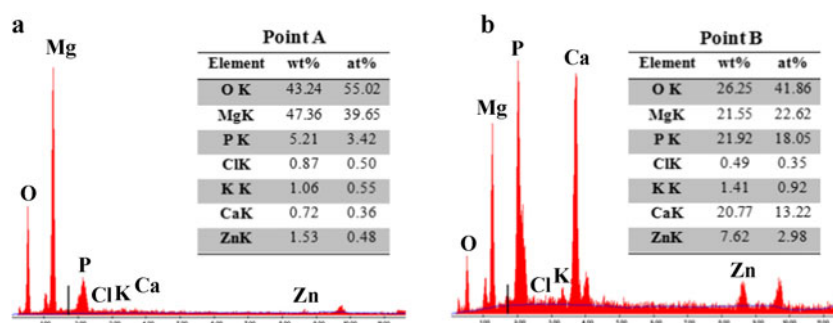


Figure 10. EDS analyses of (a) point A and (b) point B, for 3 wt% Zn immersed in SBF for 144 h.

α -Mg matrix and the anodic eutectic. The corrosion attack can be developed firstly within the eutectic and then occurs in α -Mg grain (Amira *et al* 2008). Therefore, it can be assumed that a preferential dissolution may occur resulting in increased corrosion attack of Mg₅₁Zn₂₀ phase.

Mg–9Zn suffers from heavy corrosion by formation of heterogeneous laminar corrosion products, while the inner layer is composed of Mg(OH)₂ phase. EDS analysis confirmed that the product of the inner layer contains O, C, Mg, Cl, Ca and Zn. However, the outer layer includes calcium phosphate with irregular morphology which precipitated loosely. The corresponding EDS analysis also revealed that the amount of calcium phosphate in the outer layer is significantly higher than that of the inner layer. This result is in agreement with previous finding by Song *et al* (2010).

The degradation rates (in units of mm year⁻¹) were obtained according to ASTM-G31-72. The corrosion rate is given by (8):

$$\text{Corrosion rate} = \frac{KW}{ATD}, \quad (8)$$

where the constant $K = 8.76 \times 10^4$, W is weight loss (g), A is the sample area exposed to solution (cm²), T is the exposure time (h) and D is the density of the material (g/cm⁻³). The weight loss corrosion rate of Mg–3Zn alloy was calculated and found to be 1.84 mm year⁻¹ for Mg–3Zn alloy compared to 5.19 and 2.91 mm year⁻¹ for Mg–0.5Zn and Mg–1.5Zn alloys, respectively. The results also showed that increasing Zn content in Mg alloy to 6 and 9 wt% increased the corrosion rates to 7.23 and 11.78 mm year⁻¹, respectively. These results are in good agreement with the results of Kirkland *et al* (2010).

3.4 Potentiodynamic polarization test

Potentiodynamic polarization test in Kokubo's solution was performed to assess the corrosion behaviour of Mg– x Zn alloy as shown in figure 11. From the graph, it can be seen that the hydrogen evolution (cathodic polarization) in Mg–0.5Zn is higher than the other Mg alloys containing higher Zn, which indicates that the corrosion potential (E_{corr}) is more negative (active) in 0.5 wt% Zn. The kinetic of cathodic

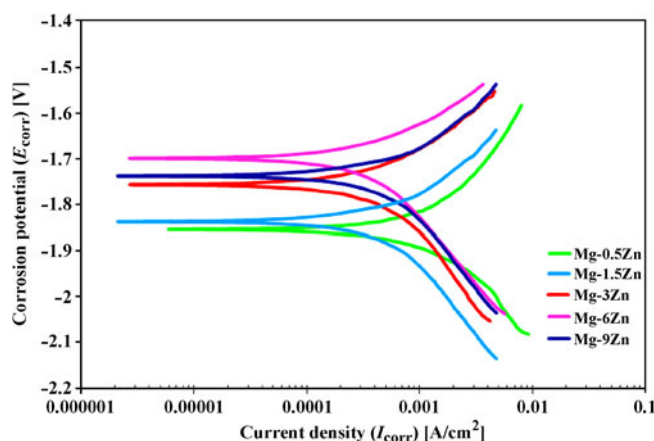


Figure 11. Potentiodynamic polarization curves of Mg–Zn alloy specimens in Kokubo solution.

reaction in Mg–0.5Zn is noticeably faster compared with other alloys with a percentage of Zn content. By addition of 3 wt% Zn to the alloy, the cathodic and anodic reactions were kinetically decreased compared to other concentrations of Zn. As shown in table 1, E_{corr} of Mg–0.5Zn is more negative than 9, 6, 3 and 1.5 wt% Zn alloy. However, the Mg–3Zn alloy showed better corrosion properties, which can be attributed to the formation of a barrier film in this alloy which is more protective.

The corrosion current density decreased from 144 $\mu\text{A}/\text{cm}^2$ in 0.5 wt% Zn to 103 $\mu\text{A}/\text{cm}^2$ in 3 wt% Zn, whereas this value for 6 and 9 wt% Zn increased to 122 and 147 $\mu\text{A}/\text{cm}^2$, respectively. This indicates higher corrosion resistance of Mg–3Zn. The presence of a higher amount of MgZn phases as confirmed by results of thermal analysis in Mg–3Zn suggests the enhanced corrosion resistance of the alloy, while formation of Mg₅₁Zn₂₀ phase in Mg–6Zn and Mg–9Zn specimens can decrease the corrosion resistance. Zhang *et al* (2009) reported that the addition of more Zn content results in an increase in the corrosion current density, I_{corr} and reduced corrosion resistance.

The linear polarization resistance, R_p , can be calculated using (9) (Liu *et al* 2010; Argade *et al* 2012), where β_a is

Table 1. Mg–xZn alloys electrochemical test results.

Alloy	E_{corr} (mV)	I_{corr} ($\mu\text{A}/\text{cm}^2$)	Co. rate (mmpy)	R_p ($\text{k}\Omega\text{cm}^2$)
Mg–0.5Zn	–1840.6	144	2.1	0.84
Mg–1.5Zn	–1740.6	134	1.67	0.99
Mg–3Zn	–1701.7	103	1.55	1.17
Mg–6Zn	–1759.9	122	1.83	0.96
Mg–9Zn	–856.8	147	2.21	0.82

the anodic and β_c is the cathodic Tafel slopes. The calculated results (table 1) showed that additions of Zn from 0.5 to 3 wt% into Mg–xZn alloy increased the R_p value from 0.84 to 1.17 $\text{k}\Omega\text{cm}^2$. However, further additions of Zn up to 9 wt% decreased the R_p value to 0.82 $\text{k}\Omega\text{cm}^2$. It is obvious that the corrosion behaviour of the alloy improved as R_p values increased with the addition of Zn up to 3 wt%:

$$R_p = \frac{\beta_a \beta_c}{2.3(\beta_a + \beta_c) i_{\text{corr}}} \quad (9)$$

As a result, it can be suggested that in the galvanic couple of Mg–3Zn, the α -Mg phase is assumed as the anode and MgZn phase is the cathode. However, in Mg–6Zn and Mg–9Zn, the $\text{Mg}_{51}\text{Zn}_{20}$ phase acts as the anode and α -Mg phase plays the cathode role. Therefore, the corrosion rate in Mg–xZn binary alloys follows this order: Mg–9Zn > Mg–0.5Zn > Mg–6Zn > Mg–1.5Zn > Mg–3Zn.

4. Conclusions

Mg alloys with various Zn content ranging from 0.5 to 9 wt% in as-cast condition were investigated in terms of microstructure, thermal analysis and corrosion behaviour. Microstructure analysis shows an evenly distributed MgZn phase for alloys with Zn content of 3 wt% or less. Another intermetallic phase $\text{Mg}_{51}\text{Zn}_{20}$ was identified with further additions of Zn up to 9 wt%. Corresponding reactions for these phases were detected via cooling curve thermal analysis. Liquid fraction (f_L^{DCP}) at the coherency point increased with increasing Zn content leading to an increase in volume fraction of the secondary phases at the end of the solidification process. T_{DCP} decreased with increasing Zn content for all the samples. Moreover, t_{DCP} did not change remarkably for 0.5–3 wt%, while it decreased from 6 to 9 wt%. The Mg–3Zn alloy exhibited the lowest degradation rate and the highest corrosion resistance compared to other alloys, hence, it is the most suitable candidate for biomedical applications.

References

Alvarez-Lopez M L, Del-Valle M D, Fernandez-Lorenzo J A, Garcia-Alonso M, Ruano M C and Escudero O A 2010 *Acta Biomater.* **6** 1763
 Amira S, Dubé D, Tremblay R and Ghali E 2008 *Mater. Charact.* **59** 1508

Argade G R, Kandasamy K, Panigrahi S K and Mishra R S 2012 *Corros. Sci.* **58** 321
 Bäckerud L, Chai G and Tamminen J 1990 *Solidification characteristics of aluminum alloys*, Vol 2: Foundry alloys, Des Plaines, Illinois, AFS/Skanaluminium
 Bakhsheshi-Rad H R, Idris M H, Kadir M R A and Farahany S 2012 *Mater. Des.* **33** 88
 Di-Mario C, Griffiths H, Goktekin O, Peeters N and Verbist B M J 2004 *J. Interv. Cardiol.* **17** 391
 El-Rahman S S A 2003 *Pharmacol. Research* **47** 189
 Erbel R et al 2007 *Lancet* **369** 1869
 Feyerabend F, Witte F and Kammal M 2006 *Tissue Eng.* **12** 3545
 Haferkamp H et al 2003 *Magnesium alloys and technology* (ed.) K U Kainer (Weinheim: WILEY-VCH Verlag GmbH & Co. KG aA) 226
 Harandi S E, Idris M H and Jafari H 2011 *Mater. Des.* **32** 2596
 Heublein B, Rohde R, Kaese V, Niemeyer M, Hartung W and Haverich A 2003 *Heart* **89** 651
 Kaya R A et al 2007 *J. Neurosurg. Spine* **6** 141
 Kirkland N T, Lespagnol J, Birbilis N and Staiger M P 2010 *Corros. Sci.* **52** 287
 Ku C H, Pioletti D P, Browne M and Gregson P J 2002 *Biomaterials* **23** 1447
 Lee Y C, Dahle A K and St John D H 2000 *Metall. Mater. Trans.* **A31** 2695
 Lévesque J, Dubé D, Fiset M and Mantovani D 2003 *Mater. Sci. Forum* **426–432** 521
 Liu M, Schmutz P, Uggowitzer P J, Song G and Atrens A 2010 *Corros. Sci.* **52** 3687
 Okamoto H 1994 *Phase Equilibria Diffusion* **15** 129
 Ren Y, Huang J, Yang K, Zhang B, Yao Z and Wang H 2005 *Acta Metallurgica Sinica* **41** 1228
 Rosalbino F, De Negri S, Saccone A, Angelini E and Delfino S 2010 *J. Mater. Sci.: Mater. Med.* **21** 1091
 Somekawa H, Singh A and Mukai T 2009 *Scr. Mater.* **60** 411
 Song G 2007 *Corros. Sci.* **46** 1696
 Song G and Song S 2006 *Adv. Eng. Mater.* **9** 298
 Song Y, Zhang S, Li J, Zhao C and Zhang X 2010 *Acta Biomater.* **6** 1736
 Stulikova I and Smola B 2010 *Mater. Charact.* **61** 952
 Waksman R et al 2009 *J. Am. Coll. Cardiol. Interv.* **2** 312
 Waksman R, Pakala R, Hellinga D, Baffour R, Kuchulakanti P and Seabron R 2005 *Eur. Heart. J.* **26** 417
 Waksman R, Pakala R, Kuchulakanti P K, Baffour R, Hellinga D and Seabron R 2006 *Catheter Cardiovasc. Interv.* **68** 607
 Wang J, Wang L, Guan S, Zhu S, Ren C and Hou S 2010 *J. Mater. Sci.: Mater. Med.* **21** 2001
 Wen C E, Yamada Y, Shimojima K, Chino Y, Hosokawa H and Mabuchi M 2004 *Mater. Lett.* **58** 357

- Witte F, Vogt H N, Cohen C, Kainer S, Willumeit K U and Feyerabend R 2008 *Curr. Opin. Solid State Mater. Sci.* **12** 63
- Witte F, Kaese V, Haferkamp H *et al* 2005 *Biomaterials* **26** 3557
- Witte F *et al* 2006 *Mater. Werkstoff.* **37** 504
- Witte F, Ulrich H, Palm C and Willbold E 2007 *J. Biomed. Mater. Res.* **A81** 757
- Xu L P, Yu G, Zhang E, Pan F and Yang K 2007 *J. Biomed. Mater. Res.* **A83** 0711
- Yang W, Zhang P, Liu J and Xue Y 2006 *J. Rare Earth* **24** 369
- Yin D S, Zhang E and Zeng S 2008 *Trans. Nonferrous Met. Soc. China* **18** 763
- Yu S, Zhang B, Wang Y, Geng L and Jiao X 2012 *Mater. Des.* **34** 58
- Yumiko N, Yukari T, Yasuhide T, Tadashi S and Yoshio I 1997 *Fundam. Appl. Toxicol.* **37** 106
- Zhang C, Zeng R, Chen R, Liu C and Gao J 2010 *Frontiers Mater. Sci. China* **4** 116
- Zhang E, Yin D, Xu L, Yang L and Yang K 2009 *Mater. Sci. Eng.* **C29** 987
- Zhang S *et al* 2010 *Acta Biomater.* **6** 626